Earth and Planetary Science Letters 377–378 (2013) 23–33

Contents lists available at SciVerse ScienceDirect

Earth and Planetary Science Letters

www.elsevier.com/locate/epsl

Spatio-temporal evolution of aseismic slip along the Haiyuan fault, China: Implications for fault frictional properties

R. Jolivet [a,*,1], C. Lasserre [a], M.-P. Doin [a], G. Peltzer [b,c], J.-P. Avouac [d], J. Sun [f], R. Dailu [e]

[a] Institut des Sciences de la Terre (ISTerre), Université Joseph Fourier – Grenoble 1, CNRS, UMR 5275, BP 53, 38041 Grenoble, France
[b] Department of Earth and Space Science, University of California, Los Angeles, United States
[c] Jet Propulsion Laboratory, California Institute of Technology, Pasadena, CA 91109, United States
[d] Tectonic Observatory, California Institute of Technology, Pasadena, CA 90125, United States
[e] Lanzhou Seismological Institute, Chinese Earthquake Administration, Lanzhou, China
[f] Institute of Geology, Chinese Earthquake Administration, Beijing, China

ARTICLE INFO

Article history:
Received 15 October 2012
Accepted 12 July 2013
Available online 25 August 2013
Editor: Y. Ricard

Keywords:
shallow creep
strike-slip fault
Tibet
SAR interferometry
frictional properties

ABSTRACT

We use 20 years of Synthetic Aperture Radar acquisitions by the ERS and Envisat satellites to investigate the spatial and temporal variations of strain rates along the 35-km long creeping section of the Haiyuan fault, at the north eastern boundary of the Tibetan plateau. We then use the derived displacements to infer the fault's frictional properties and discuss the relationship between creep and the seismic behavior of the fault. Located in between a millennial seismic gap and the 1920 M8 surface rupture trace, this section has an average creep rate of 5 ± 1 mm/yr, about the interseismic loading rate. The comparison of average surface velocity profiles derived from SAR interferometry across the creeping section reveals a creep rate increase and/or a creep migration to shallower depth between the 1990s and the 2000s. We apply a smoothed time series analysis scheme on Envisat InSAR data to investigate the creep rate variations during the 2004–2009 time period. Our analysis reveals that the creep rate accelerated in 2007, although data resolution does not allow to better constrain the onset of creep acceleration and its amplitude. Both decadal and short term transient behaviors are coeval with the largest earthquakes ($M \sim 4$–5) along the fault segment in recent years. From the precise mapping of the surface fault trace, we use the fault strike variations and the Mohr circle construction to compute the along-strike distribution of the friction coefficient along the creeping segment and compare it with the observed distribution of the creep rate. We find that the creep rate scales logarithmically with the friction coefficient, in agreement with the rate-and-state friction law in a rate strengthening regime. The estimated value of $\delta\mu/\delta \log V \sim 2 \times 10^{-3}$ indicates that the earthquakes occurring along the creeping section cannot be the cause for a significant change in the overall segment's creep rate and that the recorded micro seismicity is most likely creep-driven. Finally, given the size and frictional properties of the creeping section, we estimate, based on previous models of dynamic rupture simulations, a 0–20% probability for a rupture to break through this section. Together with the geometrical configuration of the Haiyuan fault, these results suggest that the creeping segment may act as a persistent barrier to earthquake propagation.

1. Introduction

Constraining the location and size of locked asperities along major faults is a key to a better understanding of their seismic behavior. Modern geodetic techniques, such as GPS or SAR interferometry, allow us to map the degree of locking along subduction interfaces (e.g. Mazzotti et al., 2000; Chlieh et al., 2011; Métois et al., 2012) or major strike-slip faults (e.g. Ryder and Bürgmann, 2008; Jolivet et al., 2012; Lienkaemper et al., 2012), leading to the identification of large locked asperities and estimations of the build-up rate of slip deficit to be released in future earthquakes. Locked asperities are surrounded by areas where slip mostly results from aseismic creep. Observations and modeling studies show that earthquakes tend to nucleate near the transition between locked and creeping patches and that creeping patches act as barriers to the propagation of seismic ruptures (e.g. Lapusta et al., 2000; Cattin and Avouac, 2000; Barbot et al., 2012). The numerical modeling of a frictional interface reveals that the barrier effect of an aseismic patch depends on its size and frictional properties (Kaneko et al., 2010). It is therefore of great importance to identify

* Corresponding author.
E-mail address: rjolivet@caltech.edu (R. Jolivet).
[1] Now at Tectonics Observatory, California Institute of Technology, Pasadena, CA 90125, United States.

0012-821X/$ – see front matter
http://dx.doi.org/10.1016/j.epsl.2013.07.020

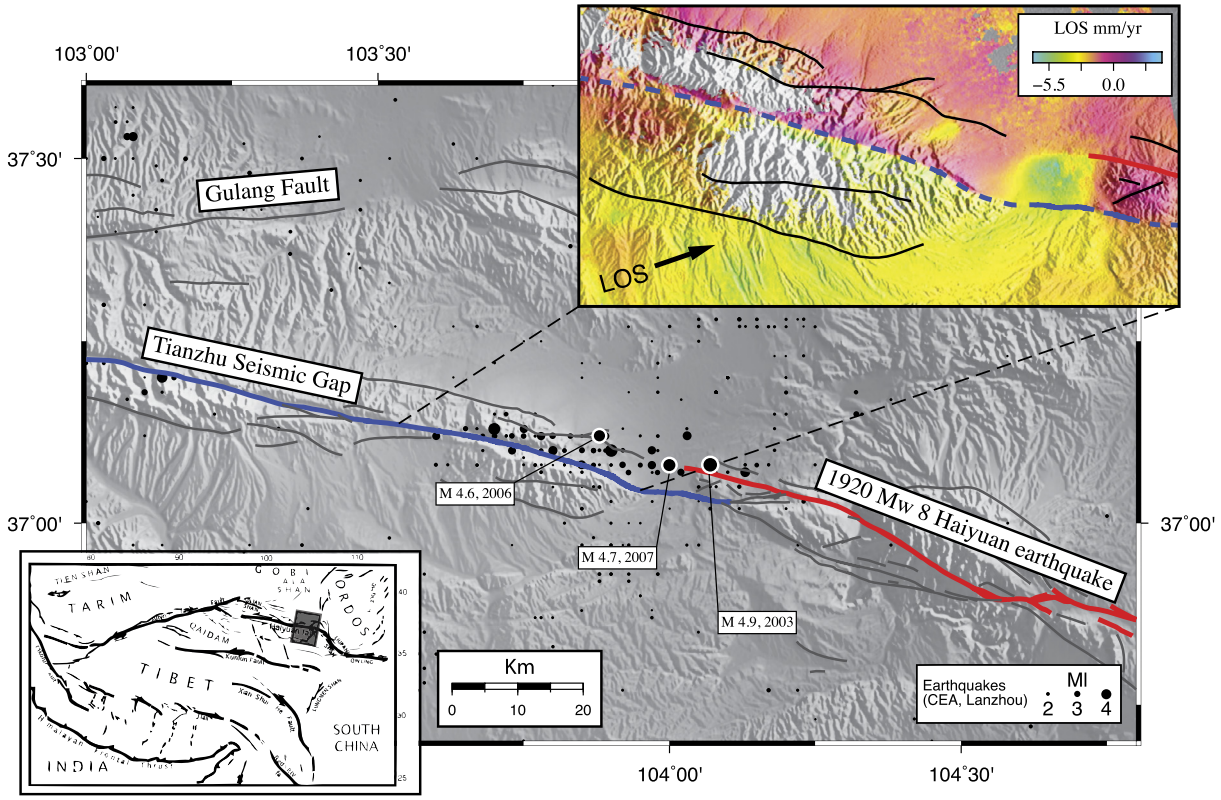

Fig. 1. Map of the seismotectonic setting along the Haiyuan Fault System. Red line is the Haiyuan 1920 M ∼ 8 earthquake surface rupture trace. Blue line is the Tianzhu seismic gap. Grey lines are secondary faults. Black dots are earthquake epicenters between 2004 and 2010 with magnitude ranging from 2.0 to 4.7 (Courtesy of Chinese Earthquake Administration, Seismological Institute of Lanzhou, M_l: local magnitude from CEA, Lanzhou). The three highlighted earthquakes are the highest recorded earthquakes during the period of InSAR observation. Bottom-Left: Regional tectonic map of the Tibetan plateau. Top-Right: Average Line-Of-Sight velocity map on Envisat track 240 spanning the 2004–2009 period from Jolivet et al. (2012). Positive range change is toward satellite. Blue dashed line is the Tianzhu seismic gap. (For interpretation of the references to color in this figure legend, the reader is referred to the web version of this article.)

creeping sections along faults and determine their lateral extension as well as their mechanical properties.

Creeping patches have been identified along several major strike-slip fault systems, such as the San Andreas Fault system (e.g. Rogers and Nason, 1971; Lisowski and Prescott, 1981; Ryder and Bürgmann, 2008), the North Anatolian fault system (Ambrasey, 1970; Çakir et al., 2005) and the Leyte fault, in the Philippines (Duquesnoy et al., 1994). Creep has been detected as well along normal faults (Doubre and Peltzer, 2007), thrust fault systems (e.g. Lee et al., 2001; Champenois et al., 2012) and subduction megathrusts (e.g. Suwa et al., 2006; Chlieh et al., 2008; Moreno et al., 2010; Loveless and Meade, 2011b; Ozawa et al., 2011). The time evolution of creep can be monitored using repeated field observations (e.g. Steinbrugge et al., 1960), creepmeters and more recently, GPS (e.g. Rolandone et al., 2008) and InSAR (e.g. Bürgmann et al., 2000; Funning et al., 2007; De Michele et al., 2011). Various temporal behaviors have been observed including steady creep (e.g. Titus et al., 2006), potentially initiated by post seismic afterslip (Çakir et al., 2012), quasi-periodic seasonal creep rate variations (e.g. Chang et al., 2009) or episodic transient creep (e.g. Lienkaemper et al., 1997, 2012). Such variability in the aseismic slip behavior affects the slip budget along faults, hence their seismic potential. Therefore, one needs not only to identify creeping patches but also to characterize their temporal evolution.

In this study, we focus on the Haiyuan Fault System (HFS), a 1000 km-long left-lateral system bounding the Tibetan plateau to the North-East (Gaudemer et al., 1995). Using a stack of sparse ERS InSAR data, Cavalié et al. (2008) revealed the existence of a narrow zone of high velocity gradient across the central section of the Haiyuan fault. They proposed that shallow creep was occurring in the brittle upper crust. From the time series analysis of densely sampled Envisat InSAR data, Jolivet et al. (2012) precisely identified a 35 km-long creeping section along the Haiyuan fault, also characterized by an intense seismic activity (Fig. 1). This section is located west of a pull-apart basin that marks the western end of the 240 km-long rupture of the 1920, M ∼ 8, Haiyuan earthquake (Zhang et al., 1987; Gaudemer et al., 1995). It also corresponds to the eastern termination of a 250 km-long millennial seismic gap, referred to as the Tianzhu seismic gap, likely at the end of its interseismic period and prone to generate M ∼ 8 earthquakes (Gaudemer et al., 1995; Liu-Zeng et al., 2007). Jolivet et al. (2012) thus showed that this creeping segment is located in between two locked fault sections at different stages of their earthquake cycle, next to a major geometric discontinuity along the fault that is thought to have played a significant role in past earthquakes rupture propagation (Liu-Zeng et al., 2007).

The shallow creep rate is estimated to be 5 ± 1 mm/yr, on average, over the 2003–2009 time span of the Envisat data (Jolivet et al., 2012). This value is consistent with the present-day loading rate, determined using GPS or InSAR data (Gan et al., 2007; Cavalié et al., 2008; Loveless and Meade, 2011a). It is also in agreement with the lower bounds of the estimated Holocene slip rates near the eastern end of the Tianzhu gap ranging between 3 and 12 mm/yr (Zhang et al., 1988; Lasserre et al., 1999; Li et al., 2009). The shallow creep rate spatial distribution, averaged over the 2003–2009 period, locally peaks up to 8 mm/yr, which overcomes the present-day tectonic loading rate at depth. This is interpreted as the signal of a temporally variable creep rate along that segment, at least during the period of observation (Jolivet et al., 2012).

In this study, we further investigate the temporal evolution of creep at the eastern end of the Tianzhu seismic gap and its rela-

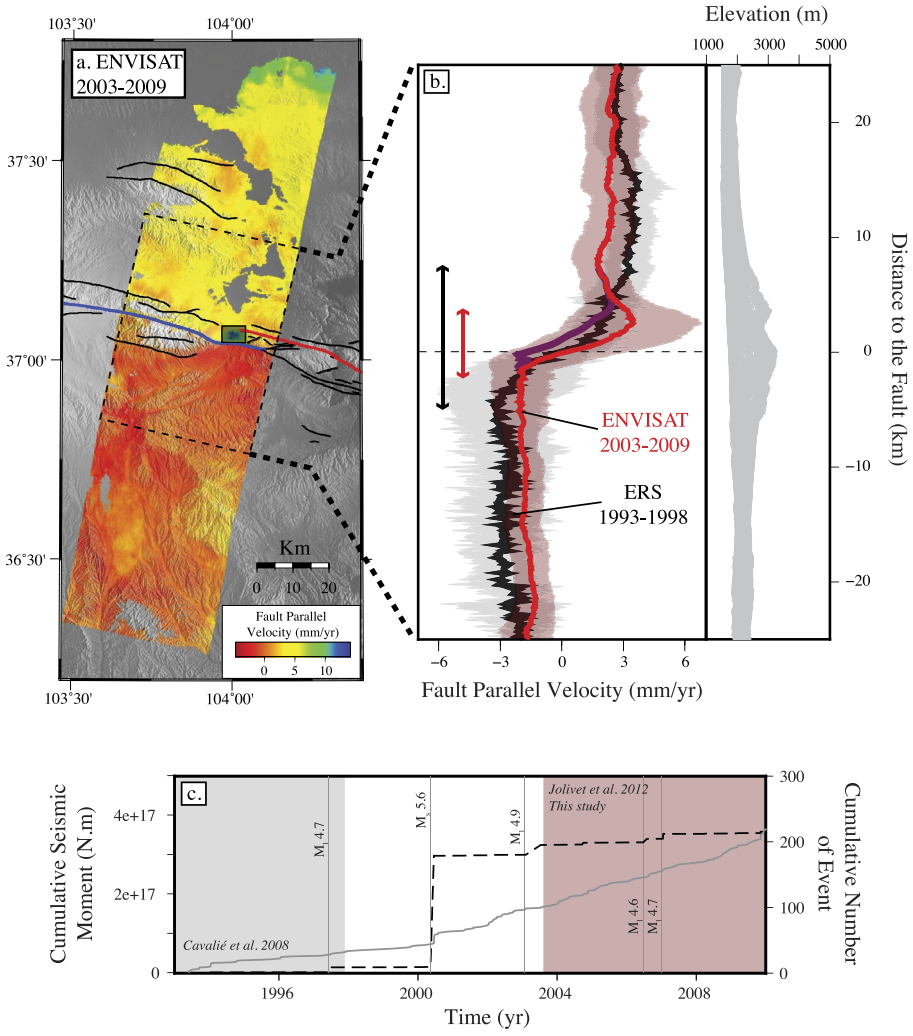

Fig. 2. a. Fault parallel velocity map across the Haiyuan fault for the 2003–2009 period averaged on the overlapping area of tracks 061 and 333 from Jolivet et al. (2012). Dashed rectangle indicates the envelope used to compute the profiles on b. Small shaded rectangle indicates the subsiding area (Jingtai basin). **b.** Fault perpendicular profiles of the fault parallel velocity. Red (resp. black) profile with associated 1-σ errors in shaded covers the 2003–2009, Envisat data, period (resp. the 1993–1998, ERS data, period). The purple profile, in the near fault zone, is similar to the red profile with the gray shaded zone, shown on a., masked out. Red (resp. black) arrows indicate a suggested width of the near-fault deforming zone. **c.** Cumulative seismic moment release and cumulative number of earthquakes between 1993 and 2010. Vertical lines indicate the largest ($M > 4.6$) earthquakes. Grey and red shaded areas indicate the periods spanned by Cavalié et al. (2008) and Jolivet et al. (2012), respectively. We use the seismic catalog provided by the Seismological Institute of Lanzhou (completion $M > 2.9$). (For interpretation of the references to color in this figure legend, the reader is referred to the web version of this article.)

tionship with the recorded seismic activity, at different time scales. We first analyze the creep rate variations at the decadal scale, comparing average surface velocity from ERS (1990s) and Envisat (2000s) data. We then evaluate the short-term evolution of the spatio-temporal distribution of surface creep using Envisat data, spanning the 2004–2009 period. Finally, we use these data to investigate the frictional properties along the fault and discuss the implications of our results for the earthquake cycle and the seismic activity of the creeping section.

2. Decadal creep rate variations and seismic activity

Comparing results from Cavalié et al. (2008) and Jolivet et al. (2012) suggests temporal variations between the two observation periods (Fig. 2). Cavalié et al. (2008) produced a profile across the Haiyuan fault of the horizontal, fault-parallel velocity, averaged over the 1993–1998 period, by stacking ERS interferograms in the overlapping area of tracks 333 and 061 (Fig. 2b). Jolivet et al. (2012) processed Envisat ASAR data using a time series analysis method on the same track 333 and 061 to produce velocity maps spanning the 2003–2009 period. Here, we assume no fault-perpendicular or vertical displacements to project onto the horizontal, fault-parallel direction, the Line-Of-Sight (hereafter LOS) velocity maps produced by Jolivet et al. (2012) on tracks 333 and 061. The average of the fault parallel velocity of both tracks in the overlapping area is shown on Fig. 2a. We then derive a profile of the fault-parallel velocity across the Haiyuan fault covering the overlapping area between tracks 333 and 061, as Cavalié et al. (2008) (Fig. 2b). Because of the larger amount of data processed by Jolivet et al. (2012) and the applied processing steps (Guillaso et al., 2006; Lopez-Quiroz et al., 2009; Doin et al., 2011), the noise level of the 2003–2009 profile (∼2 mm/yr) is smaller than that of the 1993–1998 profile (∼4 mm/yr). The comparison of both profiles suggest that the tectonic loading rate (i.e. far field displacement rate) determined from Envisat data during the 2003–2009 period (5 ± 1 mm/yr, Jolivet et al., 2012) is consistent, within uncertainties, with that from Cavalié et al. (2008) (4.2–8 mm/yr).

The high strain zone centered on the fault is narrower and shows higher peak to peak values between 2003 and 2009 than between 1993 and 1998. High velocities observed north of the

fault are due to the subsiding basin identified by Jolivet et al. (2012) (i.e. in between km 0 and 4 on the profile of Fig. 2 and hereafter called the Jingtai basin). However, the velocity profile obtained with this basin masked out (gray shaded area in Fig. 2a) still shows a higher velocity gradient across the fault. Such temporal variation in the velocity profile shape suggests that aseismic slip has migrated toward the surface and/or that the aseismic slip rate has increased between the two periods. Both may have happened simultaneously and we cannot conclude clearly on this point without any additional data. Still, the creep distribution model inferred by Jolivet et al. (2012) shows that creep reaches the surface during the 2003–2009 period, while Cavalié et al. (2008) do not see a corresponding surface velocity step across the fault. This gives some credit to the hypothesis of a migration or extension of creep toward the surface. Fig. 2c shows the evolution of the seismic moment release along the creeping segment during the 1993–2010 period. Strikingly, the biggest earthquake recorded along the creeping segment (June 6th, 2000, M_s 5.6) happened between the two observation periods and could be related to the creep migration or acceleration.

3. Short term creep rate temporal variations and seismic activity

3.1. Data processing and time series analysis

We analyze Envisat ASAR data from ascending tracks 240 and 469 and descending track 061, spanning the 2004–2009 period. For these three tracks respectively, 25, 21 and 36 acquisitions are combined into 74, 48 and 131 interferograms, using the ROI_PAC software (Rosen et al., 2004) associated with the NSBAS chain, that enhances coherence over areas with steep topography (Doin et al., 2011). The pair-wise selection of interferograms is such that each acquisition is connected to the others by at least two interferograms. Each interferogram is filtered (Goldstein and Werner, 1998), unwrapped using a cut-tree algorithm and empirically corrected from stratified tropospheric delays and residual orbital effects to maximize the signal-to-noise ratio (Cavalié et al., 2008; Doin et al., 2009). Finally, interferograms are set to a common reference. These processing steps have been extensively described by Jolivet et al. (2012). In the present study, we use the same set of interferograms to extract the temporal variations of the creep rate, while Jolivet et al. (2012) only focused on the average velocity over the 2003–2009 period. We point out that we had to exclude track 333 because of low coherence in the fault zone.

Given the expected low surface strain rates, residual phase noise due to atmospheric turbulences most likely overcomes the tectonic signal. We assume the residual Atmospheric Phase Screen (hereafter APS) is random in time. We apply a time series analysis method to estimate the contributions to the observed phase from (1) the ground deformation temporal evolution, (2) the residual APS, (3) the Digital Elevation Model (DEM) errors. Assuming that the surface deformation rate varies slowly with time, a Gaussian filter can effectively separate its signal from that of the temporally incoherent APS (Ferretti et al., 2001; Berardino et al., 2002; Schmidt et al., 2005; Hooper et al., 2007). The phase evolution through time is derived from the interferograms by solving the following linear problem independently for each pixel:

$$\Phi_{i,j} = \varphi_j - \varphi_i \quad \text{and} \quad \varphi_1 = 0, \tag{1}$$

$$\forall k \in [1, N] \quad 0 = \varphi_k - \varphi_k^s - \alpha \Delta B_k^{\perp}, \tag{2}$$

where N is the number of SAR acquisitions, $\Phi_{i,j}$ is the pixel phase value for the interferogram combining acquisitions i and j, φ_k and φ_k^s are the phase values and temporally filtered phase values (i.e. hereafter called "smoothed" phase), respectively, at the time of acquisition k, $\Delta B_k^{\perp}$ is the perpendicular baseline between acquisitions k and 1 and α is proportional to the DEM error. The APS at acquisition k is the difference $\varphi_k - \varphi_k^s$.

Model parameters (i.e. pixel phase evolution, φ_k, smoothed pixel phase evolution, φ_k^s, DEM correction, α) are inverted using the generalized least square solution for linear problems (Tarantola, 2005):

$$\mathbf{m}_{\text{post}} = \mathbf{m}_{\text{prior}} + \left(\mathbf{G}^t \mathbf{C}_{\text{D}}^{-1} \mathbf{G} + \mathbf{C}_{\text{m}}^{-1}\right)^{-1} \mathbf{G}^t \mathbf{C}_{\text{D}}^{-1} (\mathbf{d}_{\text{obs}} - \mathbf{G}\mathbf{m}_{\text{prior}}). \tag{3}$$

The vectors $\mathbf{m}_{\text{prior}}$ and $\mathbf{m}_{\text{post}}$ contain the "a priori" and "a posteriori" model parameters, respectively, with $\mathbf{m}_{\text{prior}}$ set to the null vector. The design matrix, $\mathbf{G}$, is built from Eqs. (1) and (2). The data vector, $\mathbf{d}_{\text{obs}}$, contains interferograms pixel phase values followed by zeros. We compute the variance for each dates of acquisitions by inverting the autocovariance of each interferogram in a least square scheme. The acquisition variance values are estimates of the APS noise level in each acquisition and are used in the "a priori" data covariance matrix, $\mathbf{C}_{\text{D}}$, in the lines corresponding to Eq. (2). Diagonal terms corresponding to Eq. (1) are set to a low value (i.e. 0.1 rad) and non-diagonal terms of $\mathbf{C}_{\text{D}}$ are set to zero. Phase time filtering is performed through the model covariance matrix, $\mathbf{C}_{\text{m}}$, by setting non-zero off-diagonal covariances between the smoothed phase values, φ_k^s:

$$\mathbf{C}_{\text{m}}^{i,j} = \left(\frac{\sigma_m \lambda_0}{\lambda}\right)^2 e^{\frac{-\Delta t_{i,j}}{2\lambda}}, \tag{4}$$

where, σ_m is the "a priori" phase standard deviation (higher than the order of magnitude of the expected variations, i.e. 100 rad), $\Delta t_{i,j}$ is the temporal baseline between acquisitions i and j, λ is the time correlation parameter, set to 10 yr, λ_0 is a normalizing factor set to the mean temporal baseline between two consecutive acquisitions, here ~ 0.2 yr). In $\mathbf{C}_{\text{m}}$, the model variance of the DEM correction, α, and phase evolution terms, φ_k, are set high enough to ensure no "a priori". All other terms in $\mathbf{C}_{\text{m}}$ are null (for a discussion on the model covariance parameters, see Radiguet et al., 2011). The resulting root mean square difference between observed and synthetic interferograms is 0.28 rad, 0.32 rad and 0.32 rad for the tracks 240, 469 and 061, respectively (see supplementary material). The residual uncorrelated variances at long distances are 0.08 rad^2, 0.16 rad^2 and 0.3 rad^2 for tracks 240, 469 and 061 respectively (see supplementary material).

Jolivet et al. (2012) analyzed the interseismic loading along the Haiyuan fault. It can be modeled by a 5 mm/yr left-lateral slip rate below a 20 km locking depth (consistent with the micro-seismicity distribution), using a dislocation embedded in a semi-infinite elastic medium (Savage and Burford, 1973). Additionally, they show that the estimate of shallow creep above the locking depth was poorly sensitive to this interseismic model. In the following, we use this model to correct the time series from the interseismic loading signal on each of our three tracks. This way, we can focus on the surface expression of the shallow creep. Snapshots of the resulting time series can be found in Fig. 3 while the complete time series are shown in the supplementary material (Figs. S1, S2 and S3).

3.2. Short term creep rate variations

The smoothed phase evolution shows the two main features identified by Jolivet et al. (2012) (Fig. 3a): (1) subsidence in the extensional jog, called the Jingtai basin, in between the 1920 rupture trace and the eastern Tianzhu gap; (2) a 35 km-long creeping segment extending from the Jingtai basin to the western Mao Mao Shan along the Tianzhu seismic gap. The study of the subsidence observed in the pull apart basin is out of the scope of this paper. Here, we focus on the temporal evolution of shallow creep. To

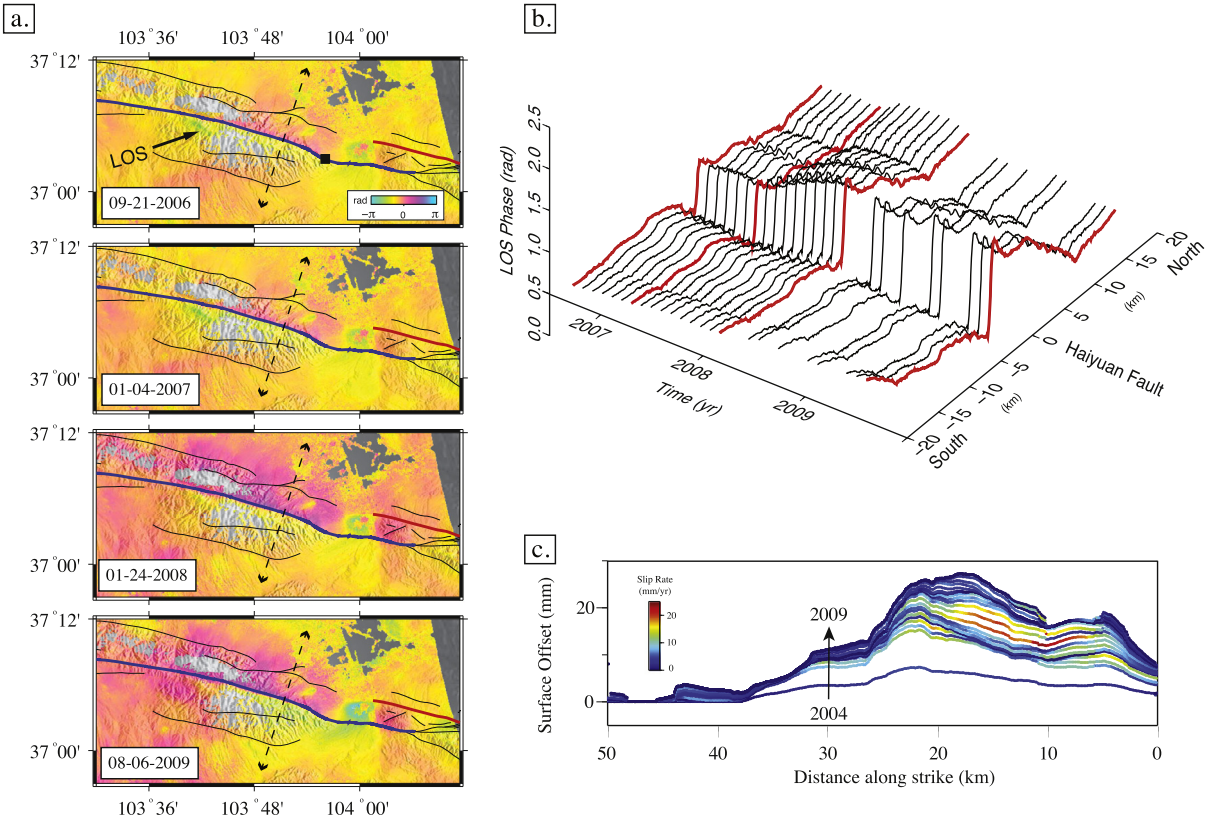

Fig. 3. a. Snapshots of the smoothed InSAR time series on Envisat ascending track 240, at acquisition dates 09/21/2006, 01/04/2007, 01/24/2008 and 08/06/2009, showing surface displacement, relative to 01/15/2004, projected along the Line-Of-Sight. Positive range change is toward satellite. Faults are as in Fig. 1. Dashed arrow indicates the location of the profile shown on panel **b.**. Thick black arrow indicates the Line-Of-Sight direction of the radar acquisition. Black square on the first snapshot is km 0 on Fig. 5. **b.** Fault perpendicular profile of Line-Of-Sight displacement across the Haiyuan fault, on track 240, as a function of time. **c.** Along-strike distribution of the fault parallel creep. Color indicates the velocity between two successive acquisitions.

increase the signal to noise ratio, we work on local profiles, perpendicular to the fault (Fig. 3). Indeed, even though such profiles are affected by APS, they are only offseted by this relatively long wavelength (∼10 km) residual noise, leaving the step across the fault un-changed. Focusing on the range change across the fault (i.e. a short spatial wavelength signal), our analysis should not be biased by atmospheric annual and pluri-annual oscillations (i.e. relatively long spatial wavelength signals).

One striking feature is the apparent creep rate change between late 2007 and 2008. Fault perpendicular profiles of the phase evolution through time clearly indicate a creep rate increase during a one year period (Fig. 3b). Profiles extracted from the "rough" phase evolution show a similar pattern, even though it is impossible to measure because of strong APS, confirming such rate increase does not result from our smoothing procedure (see supplementary material).

To test the robustness of our observation, we extract the horizontal creep rate evolution averaged over the creeping segment. We use profiles similar to the one shown on Fig. 3b to measure, along strike, at each time step of the time series on each track, the across fault step along the LOS, following an approach similar to Kaneko et al. (2012) (see supplementary material for a description). Jolivet et al. (2012) show that the creep is homogeneously distributed at depth and that vertical slip along the creeping segment is negligible and restricted to the pull-apart basin. Therefore, we assume no vertical and fault perpendicular motion to project the along-strike distribution of the creep onto the fault parallel direction and derive the corresponding along-strike distribution of creep rates. Fig. 3c shows the temporal evolution of the surface slip distribution and the corresponding creep rates measured on Envisat track 240. The creep is maximum in the center of the segment and exhibits its higher rates along the eastern section of the creeping segment (abscissa 0 to 20 km). We finally average the creep rate along strike between km 0 and 30, independently on each track.

The resulting creep rate evolution between consecutive acquisition dates, measured on each of the three tracks, is shown on Fig. 4 together with the corresponding evolution filtered in time, using a 4 months Gaussian kernel. The creep rates measured from one date to another show a large scatter, especially when the temporal sampling is fine, as the creep rate estimated between consecutive acquisitions is very sensitive to phase noise. Scatter between tracks may reflect lateral variations in creep rates, possible slight contributions from local vertical displacements and variable quality in the phase reconstruction between tracks. The consistency of the filtered rates derived from ascending and descending tracks confirms that, to the first order, most of the observed motion is indeed horizontal and parallel to the fault. Our measurements reveal an average horizontal creep rate of 2–3 mm/yr before 2007, and after 2008, significantly lower than the far field loading rates inferred by Gan et al. (2007), Cavalié et al. (2008) and Jolivet et al. (2012) from geodetic data. Given the 5 ± 1 mm/yr tectonic loading rate, such creep rate would result in a 2–3 mm/yr of slip deficit accumulated between 2004 and 2007. During the year 2007, the surface horizontal creep rate reaches 7–9 mm/yr (filtered evolution). Despite the scatter observed around these average velocities (±5 mm/yr), the average creep rate during this period significantly increases. Summarizing our observations, we state that (1) the creep rate is stable (∼2–3 mm/yr) before 2007 (±1 mm/yr) and after 2008 (±2 mm/yr), (2) a surface creep rate increase is visible and last for about a year.

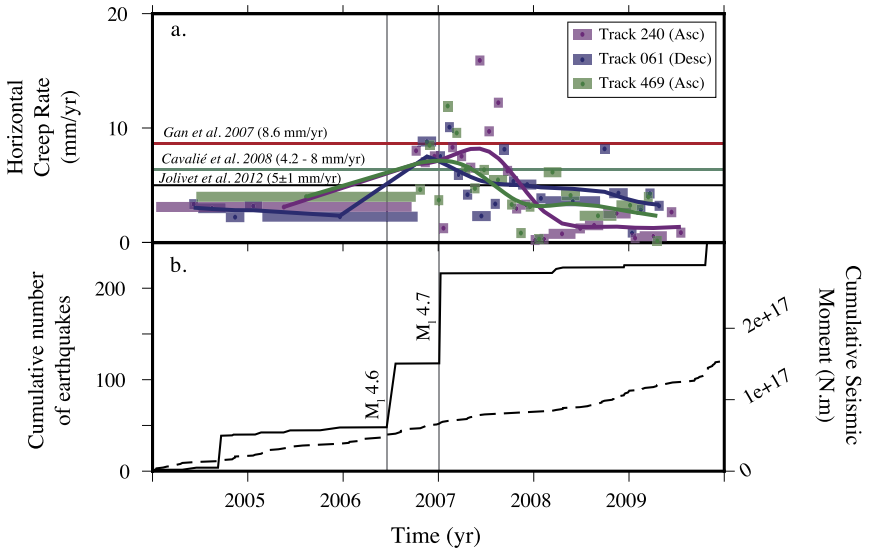

Fig. 4. a. Fault parallel creep rate, averaged along the 35 km-long creeping segment, as a function of time for ascending (Asc) tracks 240 (purple), 469 (green) and descending (Desc) track 061 (blue). Each colored box is centered on the velocity at mid-distance between two successive acquisitions and shows the time span between these two acquisitions. The continuous curves are the smoothed temporal evolution of the horizontal creep rate. Black (reps. green and red) line indicates the tectonic loading rate estimated by Jolivet et al. (2012) (resp. Cavalié et al., 2008 and Gan et al., 2007). **b.** Cumulative seismic moment (continuous line) and cumulative number of events (dashed line) during the 2004–2010 period. We note that most of the energy is released by two earthquakes of magnitude 4.6 and 4.7. (For interpretation of the references to color in this figure legend, the reader is referred to the web version of this article.)

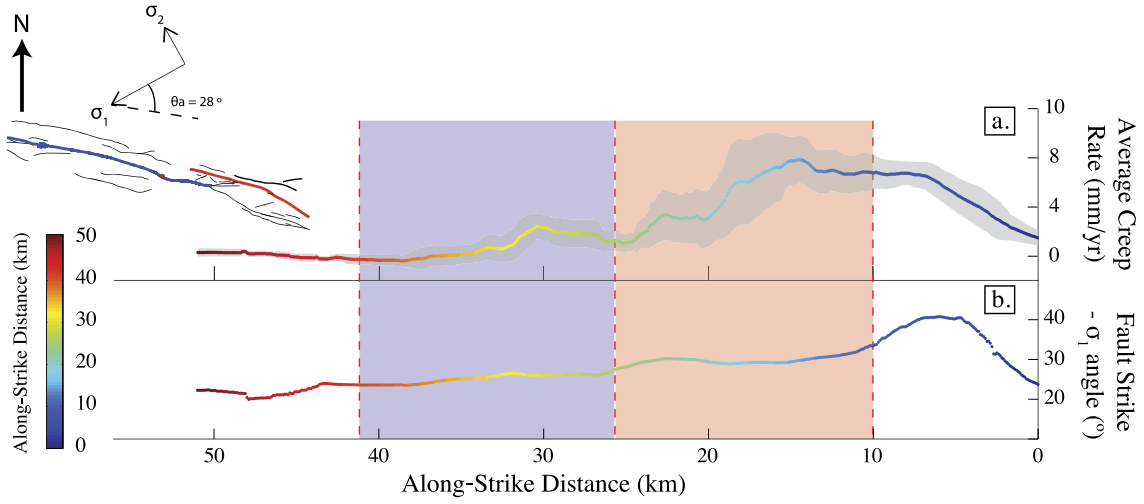

Fig. 5. a. Along-strike distribution of the average, horizontal fault parallel, creep rate measured on average velocity fields determined by Jolivet et al. (2012). The color indicates the along-strike distance from the origin point. Red and blue boxes show the limits of two different fault segments showing different frictional behavior. The sketch map on the left indicates the problem geometry, with the assumed stress orientation (blue: Tianzhu seismic gap, red: 1920 M8 rupture trace, black: secondary faults). **b.** Along-strike evolution of the angle between the local fault strike and the regional principal stress orientation, given an average angle θ_a of 28°. (For interpretation of the references to color in this figure legend, the reader is referred to the web version of this article.)

Two moderate size earthquakes happened during the Envisat observation period in July 2006 ($M_l = 4.6$) and January 2007 ($M_l = 4.7$). As shown on Fig. 4, the creep rate increase occurs during the second half of year 2006 and early 2007, coincident with the July 2006 and January 2007 earthquakes. Furthermore, the creep rate reaches its highest value soon after the January 2007 event. However, because of the temporal smoothing applied to the InSAR time series, it is hard to tell whether these earthquakes occurred before or after the beginning of the creep rate increase period. We discuss the possible relationship between the observed shallow creep and the occurrence of earthquakes in the next section, after investigating for the frictional properties of the Haiyuan fault creeping segment.

4. Discussion

4.1. Frictional properties of the creeping segment of the Haiyuan fault

Whether a fault creeps aseismically or produces episodic seismic slip events depends primarily on its frictional properties and more particularly on how friction varies with slip rate (e.g. Brace and Byerlee, 1978; Dieterich, 1979; Scholz, 1998). Assuming a uniform stress field, unperturbed by small earthquakes, the along-strike creep rate variations observed along the Haiyuan fault creeping segment could actually result from spatial variations of frictional stresses related to the fault geometry. This would then allow estimating the rate-dependency of friction. To test this hypothesis, we compare the along-strike variations of the friction

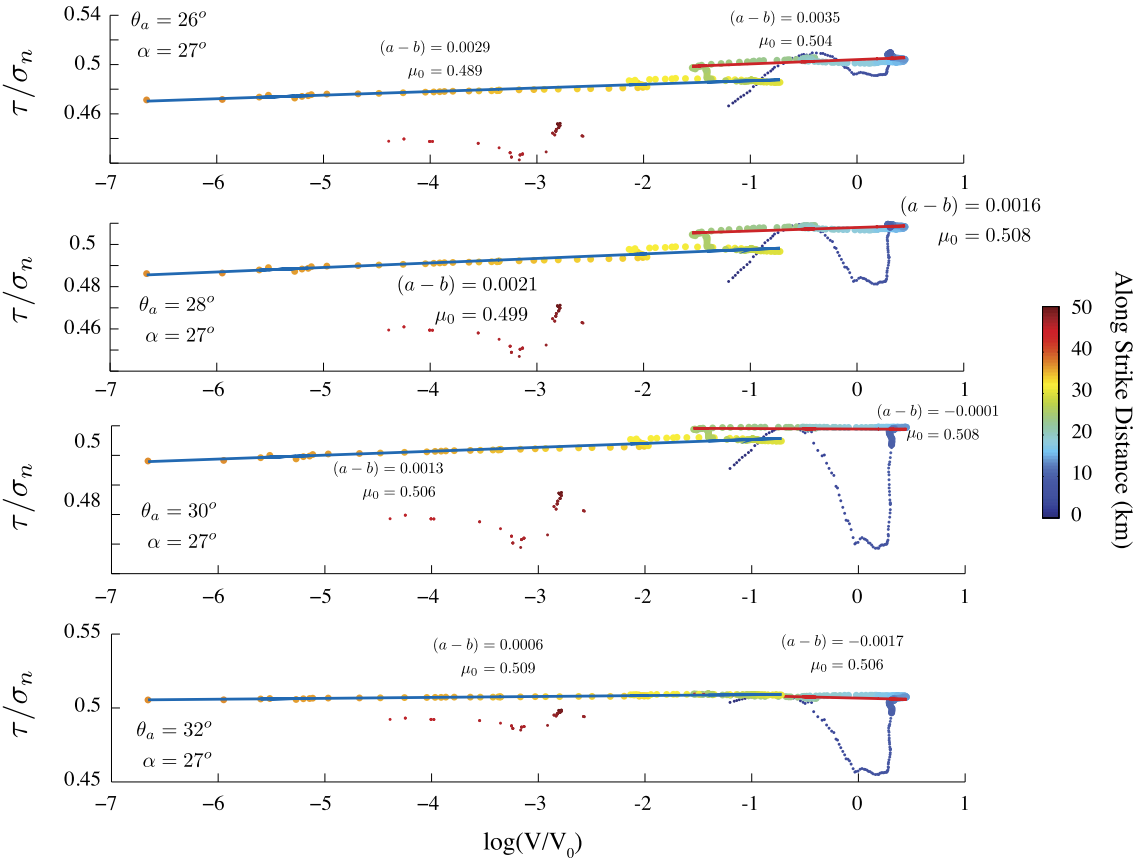

Fig. 6. Friction coefficient as a function of the log of the creep rate, averaged over the 2003–2009 period. Here, the friction coefficient is estimated assuming the angle between the principal stress σ_1 and the fault strike $\theta = 26°$, 28°, 30° and 32°, from top to bottom, and an internal friction angle $\alpha = 27°$. The blue (resp. red) line indicates the best fitting rate-and-state law for the western (resp. eastern) segment. (For interpretation of the references to color in this figure legend, the reader is referred to the web version of this article.)

coefficient with the average creep rate measured on the velocity map on Envisat track 240 from Jolivet et al. (2012). We use, every 45 m along the fault trace, a 200 m-wide, 30 km-long, fault perpendicular profile to determine the LOS creep rate variations along strike, using a similar method than in Section 3.2. These fault perpendicular profiles are akin to the one shown in Fig. 3. Assuming no vertical motion, we project the derived LOS velocity profiles onto the fault parallel direction (Fig. 5). Given the average creep rate spatial distribution derived by Jolivet et al. (2012), we will assume, in the following, a constant creep rate along dip, down to the locking depth (20 km), along a vertical fault that follows its surface trace.

Based on the Mohr circle construction, assuming that the intermediate principal stress is vertical, as implied by the strike-slip tectonic regime, the friction coefficient μ writes as

$$\mu = \frac{\tau}{\sigma_n} = \frac{R \sin 2\theta}{1 + R \cos 2\theta}, \tag{5}$$

where τ is the shear stress on the fault, σ_n is the normal stress on the fault, $R = \frac{\sigma_1 - \sigma_3}{\sigma_1 + \sigma_3}$ is equal to the sine of the internal friction angle, α (assuming cohesion is negligible) and θ is the angle between the fault strike and the direction of the maximum principal stress, σ_1. Using along-strike variations of the fault azimuth mapped on SPOT images, we compute the along strike variations of the friction coefficient along the creeping segment. The friction angle α is fixed to the ubiquitous value of 27° (Byerlee, 1978) and the principal axis of the stress field makes an angle θ_a with the average azimuth of the fault. No particular study focused on the precise orientation of σ_1 in this area, but the focal mechanisms of recent earthquakes, as well as regional strain field inferred from geodetic studies, suggest an angle of about 30° (Holt et al., 2000; Lasserre et al., 2001; Gan et al., 2007; Liu-Zeng et al., 2007). Fig. 6 shows results obtained for θ_a between 26° and 32°. To assess for the sensitivity of our analysis, we also explore a wider range of values for θ_a, between 12° and 40°, and α, between 22° and 32° (e.g. Schellart, 2000) (Fig. 7).

It has been observed in laboratory experiments and in post-seismic studies of afterslip that, in steady-state conditions, the coefficient of friction varies in proportion to the logarithm of the sliding velocity (e.g. Dieterich, 1979; Marone, 1998; Perfettini and Avouac, 2004; Hsu et al., 2006). According to the rate-and-state formalism (Dieterich, 1979; Ruina, 1983), which has shown much success in reproducing fault's behavior and modeling of geodetic datasets over one or multiple seismic cycles, including the inter-, co- and post-seismic periods on different tectonic settings, the steady-state friction coefficient μ at slip rate V can be written,

$$\mu = \mu_0 + (a-b) \log \frac{V}{V_0}, \tag{6}$$

where, V_0 is a reference slip rate (here, 5 mm/yr), μ_0 is the friction coefficient at V_0 and a and b are material properties (log refers to as the natural logarithm). If $(a-b) < 0$, an increase of the slip rate will result in a decrease of the frictional resistance along the fault plane. Segments showing such properties, referred to as "rate-weakening", allow nucleation of seismic ruptures and favor their propagation. If $(a-b) > 0$, an increase of the slip rate will result in an increase of the frictional resistance along the fault plane. Segments showing such properties, referred to as

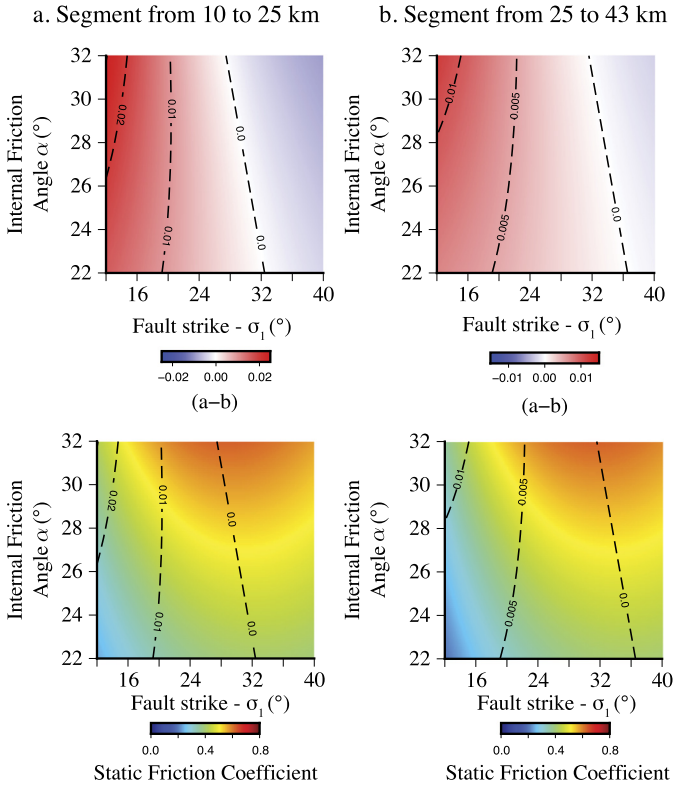

Fig. 7. Exploration of the $(a-b)$ parameter and of the static friction coefficient μ_0 along the Haiyuan fault, as a function of the internal friction angle and the principal axis of the regional stress field. **Top.** Distribution of $(a-b)$ along the segment of the Haiyuan fault located between km 10 and 26 (red on Figs. 5 and 6), to the left, and between km 26 and 43 (blue on Figs. 5 and 6), to the right. The red domain indicates rate-strengthening behavior, while the blue domain indicates rate-weakening. **Bottom** Distribution of μ_0 along the segment of the Haiyuan fault located between km 10 and 26, to the left and between km 26 and 43, to the right. Dashed lines indicate the contour lines of the $(a-b)$ parameter distribution. (For interpretation of the references to color in this figure legend, the reader is referred to the web version of this article.)

"rate-strengthening", favor aseismic slip and tend to arrest seismic rupture.

The plots in Fig. 6 show that friction varies approximately linearly with the logarithm of the sliding velocity. However, we see that in most cases the data point delineate two trends. One trend corresponds to the western segment along which creep rate is lower and quite steady (abscissa 26 km to 44 km in Figs. 3 and 5). Assuming a typical friction angle of 27° and an optimally oriented fault ($\theta_a = 28°$), this segment yields a positive $(a-b)$ value, consistent with an aseismic slip mode, of about 2.10^{-3}. This estimate falls in range of laboratory values (e.g. Marone, 1998; Carpenter et al., 2009), typically between 10^{-3} and 10^{-2}, or of values determined on natural faults from afterslip studies (e.g. Hearn et al., 2002; Miyazaki et al., 2004; Perfettini and Avouac, 2004, 2007; Fukuda et al., 2009; Hsu et al., 2006, 2009b, 2009a; Barbot et al., 2009) or from seasonal variations of creep rate (Chang et al., 2009), typically between 10^{-4} and 10^{-2}. Fig. 7b shows that our estimate varies weakly with the assumed friction angle but is more sensitive to the assumed azimuth of the maximum principal stress. This analysis shows that σ_1 needs to make an angle of less than 32–35° with the average fault azimuth (~102°N) for $(a-b)$ to be positive.

The other linear trend in Fig. 6 corresponds to the eastern segment (abscissa 0 km to 26 km in Figs. 3 and 5) along which the creep rate has been very variable over the observation period (Fig. 3c). Interestingly, that segment yields a generally lower $(a-b)$ value than along the western segment. A neutral to possibly locally negative value would be consistent with the higher and temporally more variable creep rate observed here. Indeed a quasi-neutral rate-dependency of friction on sliding rate implies a higher sensitivity to stress perturbations.

Our analysis does not bring any tight constraints on the reference friction, μ_0 in Eq. (6), as this value depends strongly on the assumed azimuth of σ_1, which is not well constrained from available observations, and on assumed value of the internal friction angle. Still, as the segment is creeping, $(a-b)$ needs to be positive (i.e. rate-strengthening). Therefore, we find that the reference friction coefficient needs to be lower than 0.7 (Fig. 7). A very low value, ~0.2, such as that measured on rock samples from the fault core of the creeping segment of the San Andreas fault would also be possible (Carpenter et al., 2011; Lockner et al., 2011).

4.2. Barrier effect of the creeping segment of the Haiyuan fault

Given such mechanical properties arise the question about the role of this segment in the past major earthquakes initiation, propagation and rupture. Fault geometry is one of the parameters controlling where large ruptures nucleate and stop (Wesnousky, 2006; Klinger, 2010). Along the Haiyuan fault, shallow creep is located west of the junction of two major fault segments, marked by a significant, km-scale, pull-apart basin, a major step-over in the fault geometry. That geometric singularity is the ending point of the 1920 M8 rupture (Zhang et al., 1987; Gaudemer et al., 1995) and is described as the limit of some earlier major ruptures, while other may have by-passed it (Liu-Zeng et al., 2007). Such characteristics makes it a good candidate for a permanent, or quasi-permanent, barrier to earthquake propagation.

Additionally, fault frictional properties do control the extension of seismic ruptures and their spatial distribution would determine the size and the timing of earthquakes over multiple cycles. From the dynamic modeling of a large number of ruptures and using the rate-and-state formalism, Kaneko et al. (2010) show that the probability for an earthquake to break through a rupture-impeding patch scales with the product of the size of the aseismic patch D and the quantity $(a-b)\sigma_n$. Assuming a normal stress σ_n about 50 to 100 MPa (i.e. $(a-b)\sigma_n$ ranges between 0.1 to 0.2 MPa) and given the length $D = 35$ km, the probability of an earthquake to break through this segment ranges between 0 and 20%. We note that this value is dependent on the model set-up chosen by Kaneko et al. (2010). The eastern section of the Haiyuan fault did rupture in 1920, and the Tianzhu seismic gap is accumulating slip since about a thousand years (Liu-Zeng et al., 2007). Therefore, although recent modeling results highlighted the role of dynamic weakening in the propagation of earthquakes through velocity strengthening segments (Noda and Lapusta, 2013), it is most likely that the next large earthquake in the area will affect the Tianzhu gap, and, given the pre-stress state, the frictional properties and the geometric discontinuity, it is most likely to be arrested at this location.

4.3. Creep rate fluctuations and micro-seismicity

As mentioned in particular by Johanson and Burgmann (2005), while locked fault segments are quiescent (excluding off-fault seismicity), creeping segments exhibit a strong micro- and moderate seismic activity, with characteristic patterns, such as repeating earthquakes (Nadeau and McEvilly, 1999) and streakes of microquakes (Rubin et al., 1999; Waldhauser et al., 2004). Here, the micro- and moderate seismic activity is coincident with the creeping zone, while the Tianzhu gap and the 1920 rupture section remain silent (Fig. 1). This observation confirms the along-strike extension of the observed creep at the surface.

Although several examples show that micro- and moderate seismic activity can be driven by aseismic slip (e.g. Rubin et al., 1999; Waldhauser et al., 2004; Lohman and McGuire, 2007), the modulation of creep by moderate size events is still a debated question. Triggered slow slip has been observed in the past following large ($M_w > 6$) earthquakes as the well known post-seismic slip (e.g. Hsu et al., 2006; Ryder et al., 2007; Perfettini et al., 2010). Onsets of creep or creep rate increase periods have also been reported following moderate size earthquakes (e.g. Murray and Segall, 2005; Lienkaemper et al., 2012). However, the mechanisms for such creep modulation are still debated. For instance, along the San Andreas fault, temporally dense EDM measurements across the creeping segment that runs from Parkfield to San Juan Batista reveals a local creep rate increase following three moderate size earthquakes ($M \sim 4.5$) along the fault plane (Murray and Segall, 2005). In that study, Murray and Segall (2005) stated that the static stress changes associated with these events were not sufficient to explain the accelerating creep episode and suggested that the triggered creep was larger than expected because of the previously stored strain on that section of the fault.

Given the frictional properties we inferred along the Haiyuan fault segment and neglecting dynamic effects, we can compute the Coulomb stress change needed for a given creep rate increase. Following Perfettini et al. (2010), we can write the Coulomb stress change, ΔCFF, as

$$\Delta CFF = (a-b)\sigma_n \log \frac{V_2}{V_1}, \quad (7)$$

where V_1 and V_2 are the creep rate before and after an earthquake, respectively. Given the fault to be under lithostatic pressure, with a density of 3×10^3 (kg/m^3), at a depth of 5 km, with $(a-b) = 2 \times 10^{-3}$, increasing the creep rate by a factor of 2 requires $\Delta CFF = 0.2$ MPa. Even though the earthquakes that could explain the observed creep rate increase are bigger than usual along that fault segment (M 4.6 and 4.7), the moment released and the area concerned by a significant variation of the Coulomb stress change are both too small to result in such high creep rate variations, at least along the western section of the creeping segment. Along the eastern section, our previous analysis suggests that $(a-b)$ could be small and resulting in a neutral behavior. This way a very small variation of the ΔCFF could induce a creep rate increase, consistent with the apparent instability of that section (Fig. 3). Following Brodsky and Prejean (2005) who suggest that slow-slip occur under lower effective stress conditions than earthquakes, a low effective normal stress along the creeping segment, resulting from a high fluid pore pressure along the fault, could explain the creep rate modulation by small earthquakes. However, to explain both the decadal creep rate increase and/or migration and the short-term creep rate increase, the stress change should have affected the whole creeping segment. Consequently, the most satisfying explanation is the case of a creep driven seismicity, with the two main events happening after, or while, creep accelerates. Still, the low temporal resolution on the onset of the creep rate increase does not allow to refine that relationship and to confirm this hypothesis.

5. Conclusion

The Haiyuan fault segment, immediately west of the section that ruptured during the 1920 M8 earthquake, has been creeping continuously over the InSAR observation periods 1993–1998 and 2003–2009. This creeping segment is about 35 km-long and the average slip rate matches approximately the long term tectonic loading rate on the fault. However, both decadal and short-term temporal variations of the surface creep rate can be observed. Spatial variations of the creep rate can be used to assess the rate dependency of fault friction. We find that our observations are, to first order, consistent with a logarithmic dependency of friction on sliding velocity and infer values of $(a-b) = \partial\mu/\partial log V$ consistent with values measured in the lab or derived from transient aseismic slip on natural faults. The eastern portion of the creeping segment shows temporal variations consistent with a lower rate-dependency of friction. These temporal creep-rate variations are coeval with seismicity fluctuations and the examination of the frictional resistance suggests that either seismicity is driven by aseismic slip or that this segment has indeed a very low $(a-b)$ value and is therefore extremely sensitive to small stress perturbations.

Although fault geometry, such as kinks or stepovers, may play a role in earthquake segmentation in general (Wesnousky, 2006), spatial variations of rheological properties is another key factor (Kaneko et al., 2010). These two factors might have contributed to the arrest of the 1920 rupture to the west. In any case, given its width and today's low coupling, it is probable that, assuming the creeping segment of the Haiyuan fault keeps creeping at such rates, it will act as a barrier to the propagation of the next earthquake.

Acknowledgements

The SAR data set was provided by the European Space Agency (ESA) in the framework of the Dragon 2 program (ID 2509 and 5305). This program also supported R. Jolivet's work, through the Young Scientist fellowship. Funding was provided by the French "Extraction et Fusion d'Information et de Données d'Interférométrie Radar" program (EFIDIR, ANR, France) and Programme National de Télédétection Spatiale (CNES). Part of G. Peltzer's contribution was done at the Jet Propulsion Laboratory, California Institute of Technology under contract with NASA. This research was partially funded by the Gordon and Betty Moore Foundation through Grant GBMF 423.01 to the Tectonics Observatory. This Tectonics Observatory contribution #234. Figures and map were prepared using Generic Mapping Tools software (Wessel and Smith, 1995).

Appendix A. Supplementary material

Supplementary material related to this article can be found online at http://dx.doi.org/10.1016/j.epsl.2013.07.020.

References

Ambrasey, N.N., 1970. Some characteristic features of Anatolian fault zone. Tectonophysics 9 (2–3).
Barbot, S., Fialko, Y., Bock, Y., 2009. Postseismic deformation due to the M_w 6.0 2004 Parkfield earthquake: Stress-driven creep on a fault with spatially variable rate-and-state friction parameters. J. Geophys. Res. 114, B07405.
Barbot, S., Lapusta, N., Avouac, J.P., 2012. Under the hood of the earthquake machine: Toward predictive modeling of the seismic cycle. Science 336 (6082), 707–710.
Berardino, P., Fornaro, G., Lanari, R., Santosti, E., 2002. A new algorithm for surface deformation monitoring based on small baseline differential SAR interferograms. IEEE Trans. Geosci. Remote Sens. 40 (11), 2375–2383.
Brace, W.F., Byerlee, J.D., 1978. Stick-slip as a mechanism for earthquakes. Science 153 (3739), 990–992.
Brodsky, E.E., Prejean, S.G., 2005. New constraints on mechanisms of remotely triggered seismicity at long valley caldera. J. Geophys. Res. 110, B04302.
Bürgmann, R., Schmidt, D.A., Nadeau, R.M., d'Alessio, M.A., Fielding, E.J., Manaker, D., McEvilly, T.V., Murray, M.H., 2000. Earthquake potential along the northern Hayward fault, California. Science 289 (5482), 1178–1182.
Byerlee, J.D., 1978. Friction of rocks. Pure Appl. Geophys. 116 (4–5), 615–626.
Çakir, Z., Akoglu, A., Belabbes, S., Ergintav, S., Meghraoui, M., 2005. Creeping along the Ismetpasa section of the North Anatolian fault (Western Turkey): Rate and extent from InSAR. Earth Planet. Sci. Lett. 238 (1–2), 225–234.
Çakir, Z., Ergintav, S., Ozener, H., Dogan, U., Akoglu, A., Meghraoui, M., Reilinger, R.E., 2012. Onset of aseismic creep on major strike-slip faults. Geology 40, 1115–1118.

Carpenter, B.M., Marone, C., Saffer, D.M., 2009. Frictional behavior of materials in the 3d SAFOD volume. Geophys. Res. Lett. 36 (5).
Carpenter, B.M., Marone, C., Saffer, D.M., 2011. Weakness of the San Andreas fault revealed by samples from the active fault zone. Nat. Geosci. 4 (4), 251–254.
Cattin, R., Avouac, J.-P., 2000. Modeling mountain building and the seismic cycle in the Himalaya of Nepal. J. Geophys. Res. 105 (B6), 13389–13407.
Cavalié, O., Lasserre, C., Doin, M.P., Peltzer, G., Sun, J., Xu, X., Shen, Z.K., 2008. Measurement of interseismic strain across the Haiyuan fault (Gansu, China), by InSAR. Earth Planet. Sci. Lett. 275 (3–4), 246–257.
Champenois, J., Fruneau, B., Pathier, E., Deffontaines, B., Lin, K.C., Hu, J.C., 2012. Monitoring of active tectonic deformations in the Longitudinal Valley (Eastern Taiwan) using Persistent Scatterer InSAR method with ALOS PALSAR data. Earth Planet. Sci. Lett. 337–338, 144–155.
Chang, S.-H., Wang, W.-H., Lee, J.-C., 2009. Modelling temporal variation of surface creep on the Chihshang fault in eastern Taiwan with velocity-strengthening friction. Geophys. J. Int. 176 (2), 601–613.
Chlieh, M., Avouac, J.P., Sieh, K., Natawidjaja, D.H., Galetzka, J., 2008. Heterogeneous coupling of the Sumatran megathrust constrained by geodetic and paleogeodetic measurements. J. Geophys. Res. 113 (B5).
Chlieh, M., Perfettini, H., Tavera, H., Avouac, J.P., Remy, D., Nocquet, J.-M., Rolandone, F., Bondoux, F., Gabalda, G., Bonvalot, S., 2011. Interseismic couping and seismic potential along the central Andes subduction zone. J. Geophys. Res. 116 (B12).
De Michele, M., Raucoules, D., Rolandone, F., Briole, P., Salichon, J., Lemoine, A., Aochi, H., 2011. Spatiotemporal evolution of surface creep in the Parkfield region of the San Andreas fault (1993–2004) from synthetic aperture radar. Earth Planet. Sci. Lett. 308 (1–2), 141–150.
Dieterich, J.H., 1979. Modeling of rock friction: 1. experimental results and constitutive equations. J. Geophys. Res. 84, 2161–2168.
Doin, M.P., Guillaso, S., Jolivet, R., Lasserre, C., Lodge, F., Ducret, G., Grandin, R., 2011. Presentation of the small baseline NSBAS processing chain on a case example: the Etna deformation monitoring from 2003 to 2010 using Envisat data. In: Proceedings of the European Space Agency Symposium "Fringe". Frascati, Italy.
Doin, M.P., Lasserre, C., Peltzer, G., Cavalié, O., Doubre, C., 2009. Corrections of stratified tropospheric delays in SAR interferometry: Validation with global atmospheric models. J. Appl. Geophys. 69 (1 Sp. Iss. SI), 35–50.
Doubre, C., Peltzer, G., 2007. Fluid-controlled faulting process in the Asal Rift, Djibouti, from 8 yr of radar interferometry observations. Geology 35 (1), 69–72.
Duquesnoy, T., Barrier, E., Kasser, M., Aurelio, M., Gaulon, R., Punongbayan, R.S., Rangin, C., 1994. Detection of creep along the Philippine fault: First results of geodetic measurements on Leyte island, central Philippine. Geophys. Res. Lett. 21 (11), 975–978.
Ferretti, A., Prati, C., Rocca, F., 2001. Permanent scatterers in SAR interferometry. Geosci. Remote Sens. 39 (1), 8–20.
Fukuda, J., Johnson, K., Larson, K.M., Miyazaki, S., 2009. Fault friction parameters inferred from the early stages of afterslip following the 2003 Tokachi-Oki earthquake. J. Geophys. Res. 114, B04412.
Funning, G.J., Bürgmann, R., Ferretti, A., Novali, F., Fumagalli, A., 2007. Creep on the Rodgers creek fault, northern San Francisco bay area from 10 year ps-InSAR dataset. Geophys. Res. Lett. 34, L19306.
Gan, W., Zhang, P.Z., Shen, Z.-K., Niu, Z., Wang, M., Wan, Y., Zhou, D., Cheng, J., 2007. Present-day crustal motion within the Tibetan Plateau inferred from GPS measurements. J. Geophys. Res. 112 (B8).
Gaudemer, Y., Tapponier, P., Meyer, B., Peltzer, G., Guo, S., Chen, Z., Dai, H., Cifuentes, I., 1995. Partitioning of crustal slip between linked, active faults in the eastern Qilian Shan, and evidence for a major seismic gap, the 'Tianzhu Gap', on the western Haiyuan Fault, Gansu (China). Geophys. J. Int. 120 (3), 599–645.
Goldstein, R.M., Werner, C.L., 1998. Radar interferogram filtering for geophysical applications. Geophys. Res. Lett. 25 (21), 4035–4038.
Guillaso, S., Reigber, A., Ferro-Famil, L., Pottier, E., 2006. Range resolution improvement of airborne SAR images. IEEE Geosci. Remote Sens. Lett. 3 (1), 135–139.
Hearn, E.H., Bürgmann, R., Reilinger, R.E., 2002. Dynamics of Izmit earthquake postseismic deformation and loading of the Düzce earthquake hypocenter. Bull. Seismol. Soc. Am. 92 (1), 172–193.
Holt, W.E., Chamot-Rooke, N., Le Pichon, X., Haines, A.J., Shen-Tu, B., Ren, J., 2000. Velocity field in Asia inferred from quaternary fault slip rates and global positioning system observations. J. Geophys. Res. 105 (B8), 19185–19209.
Hooper, A., Segall, P., Zebker, H., 2007. Persistent scatterer interferometric synthetic aperture radar for crustal deformation analysis, with application to Volcán Alcedo, Galápagos. J. Geophys. Res. 112 (B7).
Hsu, Y.-J., Avouac, J.-P., Yu, S.-B., Chang, C.-H., Wu, Y.-M., Woessner, J., 2009a. Spatiotemporal slip, and stress level on the faults within the western foothills of Taiwan: Implications for fault frictional properties. Pure Appl. Geophys. 166 (10–11), 1853–1884.
Hsu, Y.-J., Simons, M., Avouac, J.-P., Galetzka, J., Sieh, K., Chlieh, M., Natawidjaja, D.H., Prawirodirdjo, L., Bock, Y., 2006. Frictional afterslip following the 2005 Nias-Simeulue earthquake, Sumatra. Science 312 (5782), 1921–1925.
Hsu, Y.-J., Yu, S.B., Chen, H.-Y., 2009b. Coseismic and postseismic deformation associated with the 2003 Chengkung, Taiwan, earthquake. Geophys. J. Int. 176 (2), 420–430.
Johanson, I., Burgmann, R., 2005. Creep and quakes on the northern transition zone of the San Andreas fault from GPS and InSAR data. Geophys. Res. Lett. 32 (14).
Jolivet, R., Lasserre, C., Doin, M.-P., Guillaso, S., Peltzer, G., Dailu, R., Sun, J., Shen, Z.-K., Xu, X., 2012. Shallow creep on the Haiyuan fault revealed by InSAR. J. Geophys. Res. 117 (B6).
Kaneko, Y., Avouac, J.-P., Lapusta, N., 2010. Towards inferring earthquake patterns from geodetic observations of interseismic coupling. Nat. Geosci. 3, 363–368.
Kaneko, Y., Fialko, Y., Sandwell, D.T., Tong, X., Furuya, M., 2012. Interseismic deformation and creep along the central section of the North Anatolian fault (Turkey): InSAR observations and implications for rate-and-state friction properties. J. Geophys. Res. 118.
Klinger, Y., 2010. Relation between continental strike-slip earthquake segmentation and thickness of the crust. J. Geophys. Res. 115, B07306.
Lapusta, N., Rice, J.R., Ben-Zion, Y., Zheng, G., 2000. Elastodynamic analysis for slow tectonic loading with spontaneous rupture episodes on faults with rate-and-state-dependent friction. J. Geophys. Res. 105 (B10), 23765–23789.
Lasserre, C., Bukchin, B., Bernard, P., Tapponnier, P., Gaudemer, Y., Mostinsky, A., Dailu, R., 2001. Source parameters and tectonic origin of the 1996 June 1 Tianzhu ($M_w = 5.2$) and 1995 July 21 Yongden ($M_w = 5.6$) earthquakes near the Haiyuan fault (Gansu, China), China. Geophys. J. Int. 144 (1), 206–220.
Lasserre, C., Morel, P.H., Gaudemer, Y., Tapponnier, P., Ryerson, F.J., King, G., Metivier, F., Kasser, M., Kashgarian, M., Baichi, L., Taiya, L., Daoyang, Y., 1999. Postglacial left slip rate and past occurrence of M 8 earthquakes on the western Haiyuan fault, Gansu, China. J. Geophys. Res. 104 (B8), 17633–17651.
Lee, J.-C., Angelier, J., Chu, H.T., Hu, J.C., Jeng, F.S., 2001. Continuous monitoring of an active fault in a plate suture zone: a creepmeter study of the Chihshang fault, eastern Taiwan. Tectonophysics 333, 221–240.
Li, C., Zhang, P.Z., Yin, J., Min, W., 2009. Late quaternary left-lateral slip rate of the Haiyuan fault, northeastern margin of the Tibetan plateau. Tectonics 28 (5).
Lienkaemper, J.J., Galehouse, J.S., Simpson, R.W., 1997. Creep response of the Hayward fault to stress changes caused by the Loma Prieta earthquake. Science 276 (5321), 2014–2016.
Lienkaemper, J.J., McFarland, F.S., Simpson, R.W., Bilham, R., Ponce, D.A., Boatwright, J.J., Caskey, S.J., 2012. Long-term creep rates on the Hayward fault: evidence for controls on the size and frequency of large earthquakes. Bull. Seismol. Soc. Am. 102 (1), 31–41.
Lisowski, M., Prescott, W.H., 1981. Short-range distance measurements along the San Andreas fault system in central California, 1975 to 1979. Bull. Seismol. Soc. Am. 71 (5), 1607–1624.
Liu-Zeng, J., Klinger, Y., Xu, X., Lasserre, C., Chen, G., Chen, W., Tapponnier, P., Zhang, B., 2007. Millennial recurrence of large earthquakes on the Haiyuan fault near Songshan, Gansu Province, China. Bull. Seismol. Soc. Am. 97 (1), 14–34.
Lockner, D.A., Morrow, C., Moore, D., Hickman, S., 2011. Low strength of deep San Andreas fault gouge from SAFOD core. Nature 472, 82–85.
Lohman, R.B., McGuire, J.J., 2007. Earthquake swarms driven by aseismic creep in the Salton Trough, California. J. Geophys. Res. 112 (B4).
Lopez-Quiroz, P., Doin, M.-P., Tupin, F., Briole, P., Nicolas, J.-M., 2009. Time series analysis of Mexico City subsidence constrained by radar interferometry. J. Appl. Geophys. 69 (1), 1–15.
Loveless, J., Meade, B., 2011a. Partitioning of localized and diffuse deformation in the Tibetan plateau from joint inversions of geologic and geodetic observations. Earth Planet. Sci. Lett. 303 (1–2), 11–24.
Loveless, J.P., Meade, B.J., 2011b. Spatial correlation of interseismic coupling and coseismic rupture extent of the 2011 $M_w = 9.0$ Tohoku-Oki earthquake. Geophys. Res. Lett. 38 (17).
Marone, C., 1998. Laboratory-derived friction laws and their application to seismic faulting. Annu. Rev. Earth Planet. Sci. 26, 643–696.
Mazzotti, S., Le Pichon, X., Henry, P., Miyazaki, S., 2000. Full interseismic locking of the Nankai and Japan-west Kurile subduction zone: and analysis of uniform elastic strain accumulation in Japan constrained by permanent GPS. J. Geophys. Res. 105 (B6), 13159–13177.
Métois, M., Socquet, A., Vigny, C., 2012. Interseismic coupling, segmentation and mechanical behavior of the central Chile subduction zone. J. Geophys. Res. 117 (B3).
Miyazaki, S., Segall, P., Fukuda, J., Kato, T., 2004. Space time distribution of afterslip following the 2003 Tokachi-Oki earthquake: Implications for variations in fault zone frictional properties. Geophys. Res. Lett. 31 (L06623).
Moreno, M., Rosenau, M., Oncken, O., 2010. 2010 Maule earthquake slip correlates with pre-seismic locking of Andean subduction zone. Nature 467 (198), 198–202.
Murray, J.R., Segall, P., 2005. Spatiotemporal evolution of a transient slip event on the San Andreas fault near Parkfield, California. J. Geophys. Res. 110, B09407.
Nadeau, R.M., McEvilly, T.V., 1999. Fault slip rates at depth from recurrence intervals of repeating microearthquakes. Science 285, 718.
Noda, H., Lapusta, N., 2013. Stable creeping fault segments can become destructive as a result of dynamic weakening. Nature 493, 518–521.
Ozawa, S., Nishimura, T., Suito, H., Kobayashi, T., Tobita, M., Imakiire, T., 2011. Coseismic and postseismic slip of the 2011 magnitude-9 Tohoku-Oki earthquake. Nature 475 (373), 373–376.
Perfettini, H., Avouac, J.-P., 2004. Postseismic relaxation driven by brittle creep: A possible mechanism to reconcile geodetic measurements and the decay rate of aftershocks, application to the Chi-Chi earthquake, Taiwan. J. Geophys. Res. 109, B02304.

Perfettini, H., Avouac, J.P., 2007. Modeling afterslip and aftershocks following the 1992 Landers earthquake. J. Geophys. Res. 112, B07409.
Perfettini, H., Avouac, J.-P., Tavera, H., Kositsky, A., Nocquet, J.-M., Bondoux, F., Chlieh, M., Sladen, A., Audin, L., Farber, D.L., Soler, P., 2010. Seismic and aseismic slip on the Central Peru megathrust. Nature 465 (7294), 78–81.
Radiguet, M., Cotton, F., Vergnolle, M., Campillo, M., Valette, B., Kostoglodov, V., Cotte, N., 2011. Spatial and temporal evolution of a long term slow slip event: the 2006 Guerrero Slow Slip Event. Geophys. J. Int. 184 (2), 816–828.
Rogers, T.H., Nason, R.C., 1971. Active displacement on the Calaveras fault zone at Hollister, California. Bull. Seismol. Soc. Am. 61 (2), 399–416.
Rolandone, F., Burgmann, R., Agnew, D.C., Johanson, I.A., Templeton, D.C., d'Alessio, M.A., Titus, S.J., DeMets, C., Tikoff, B., 2008. Aseismic slip and fault-normal strain along the central creeping section of the San Andreas fault. Geophys. Res. Lett. 35 (14).
Rosen, P., Hensley, S., Peltzer, G., Simons, M., 2004. Updated repeat orbit interferometry package released. Eos Trans. AGU 85 (5), 47.
Rubin, A., Gillard, D., Got, J., 1999. Streaks of microearthquakes along creeping faults. Nature 400 (6745), 635–641.
Ruina, A., 1983. Slip instability and state variable friction laws. J. Geophys. Res. 88 (B12), 10,359–10,370.
Ryder, I., Bürgmann, R., 2008. Spatial variations in slip deficit on the central San Andreas fault from InSAR. Geophys. J. Int. 175 (3), 837–852.
Ryder, I., Parsons, B., Wright, T.J., Funning, G.J., 2007. Post-seismic motion following the 1997 Manyi (Tibet) earthquake: InSAR observations and modeling. Geophys. J. Int. 169 (3), 1009–1027.
Savage, J.C., Burford, R.O., 1973. Geodetic determination of relative plate motion in central California. J. Geophys. Res. 78, 832–845.
Schellart, W.P., 2000. Shear test results for cohesion and friction coefficients for different granular materials: scaling and implications for their usage in analogue modelling. Tectonophysics 324 (1–2), 1–16.
Schmidt, D.A., Burgmann, R., Nadeau, R.M., d'Alessio, M., 2005. Distribution of aseismic slip rate on the Hayward fault inferred from seismic and geodetic data. J. Geophys. Res. 110 (B8).
Scholz, C.H., 1998. Earthquakes and friction laws. Nature 391, 37–42.
Steinbrugge, K.V., Zacher, E.G., Tocher, D., Whitten, C.A., Claire, C.N., 1960. Creep on the San Andreas fault. Bull. Seismol. Soc. Am. 50 (3), 389–415.
Suwa, Y., Miura, S., Hasegawa, A., Sato, T., Tachibana, K., 2006. Interplate coupling beneath NE Japan inferred from three-dimensional displacement field. J. Geophys. Res. 111, B004402.
Tarantola, A., 2005. Inverse Problem Theory and Methods for Model Parameter Estimation. SIAM.
Titus, S.J., DeMets, C., Tikoff, B., 2006. Thirty-five-year creep rate for the creeping segment of the San Andreas Fault and the effects of the 2004 Parkfield earthquake: Constraints from alignment arrays, continuous Global Positioning System, and creepmeters. Bull. Seismol. Soc. Am. 96 (4B), S250–S268.
Waldhauser, F., Ellsworth, W.L., Schaff, D.P., Cole, A., 2004. Streaks, multiplets, and holes: High-resolution spatio-temporal behavior of Parkfield seismicity. Geophys. Res. Lett. 31 (18).
Wesnousky, S.G., 2006. Predicting the endpoints of earthquake ruptures. Nature 444 (7117), 358–360.
Wessel, P., Smith, W., 1995. New version of the generic mapping tools released. Eos Trans. AGU 76, 329.
Zhang, W.Q., Jiao, D.C., Zhang, P.Z., Molnar, P., Burchfield, B.C., Deng, Q.D., Wang, Y.P., Song, F.M., 1987. Displacement along the Haiyuan fault associated with the great 1920 Haiyuan, China, earthquake. Bull. Seismol. Soc. Am. 77 (1), 117–131.
Zhang, P.Z., Molnar, P., Burchfield, B.C., Royden, L., Wang, Y.P., Deng, Q.D., Song, F.M., Zhang, W.Q., Jiao, D.C., 1988. Bounds on the Holocene slip rate of the Haiyuan Fault, North-Central China. Quat. Res. 30 (2), 151–164.